Deformation and instability of sessile soap bubbles in an electric field

Hongsik Kim [*] and Sunghwan Jung [†]
Biological and Environmental Engineering, Cornell University, Ithaca, New York 14853, USA

(Received 17 April 2026; accepted 30 June 2026; published 22 July 2026)

Interfacial deformation under electric fields is a common phenomenon in many industrial processes. Particularly, we are interested in the dynamics of sessile soap bubbles in a parallel-plate electric field which exhibits a stable deformation regime followed by conical instability. Using side-view imaging, we track the equilibrium shapes, the transition to the unstable regime, and the pre-jet apex dynamics within one experimental system. In the stable regime, the meridional profile is well described by an ellipsoid-of-revolution fit, and the aspect ratio collapses across initial bubble sizes onto a single steady-state branch when plotted against the dimensionless field $E^* = \sqrt{\mathrm{Bo}_e}$ for data acquired within a fixed ambient session where the electric Bond number Bo_e is defined as $\varepsilon_0 E_0^2 R_0/(2\gamma)$. The end point of this branch marks the transition to the unstable regime. Above the onset of instability, the apex sharpens into a cone with half-angle $30.0^\circ \pm 0.6^\circ$, below the classical Taylor value. We interpret this smaller angle as a dynamic pre-jet angle rather than as a modified static Taylor-cone angle. To quantify the late pre-jet stage, we define the axial distance $\ell(t)$ from the instantaneous apex to a fixed reference vertex determined from the terminal cone geometry and measure its evolution. The corresponding rate grows as jetting is approached, and a near-tip inertia-capillary model captures the observed logarithmic trend as an approximation. Together, these measurements establish a single-system experimental benchmark in which stable electrocapillary deformation is organized by a single steady-state branch that leads into conical instability and pre-jet dynamics.

DOI: 10.1103/2797-3fsr

I. INTRODUCTION

Electric fields deform fluid interfaces through Maxwell stress acting against capillary pressure. The same balance underlies electrosprays, electrospinning, tip streaming, and cone-jet atomization, and it has been analyzed through classical electrohydrodynamics, reduced theories, and modern reviews of cone-jet operation [1–8]. These responses are also attractive because they enable contact-free control of charge transport and liquid delivery with high precision in electrospray ionization, particle synthesis, and thin-film deposition [9–14]. For initially smooth interfaces, a common sequence is steady deformation, loss of equilibrium, and the formation of pointed tips, jets, or bursts [15–21].

A classical reference point is Taylor's conical construction, which yields the well-known half-angle of 49.3° for an equipotential cone in a compatible electrostatic field [2]. That result, however, belongs to an idealized limit. Subsequent analyses have emphasized that cone-like critical shapes need not be unique and that field geometry, boundary conditions, and charge transport can modify the observed angle and the route to jetting [22–25]. Related analyses of conical-point solutions for liquid-liquid interfaces and of surface-attached droplets in strong electric fields further show that

[*]Contact author: hk866@cornell.edu
[†]Contact author: sj737@cornell.edu

 ©2026 American Physical Society

selected cone angles and jetting pathways depend sensitively on electrical properties, geometry, and attachment conditions [26,27]. In particular, Yarin *et al.* argued that the Taylor cone does not represent a unique critical shape and reported experimentally observed half-angles closer to non-Taylor critical solutions in parallel capacitor-like geometries [23]. A separate line of work emphasizes that cones forming dynamically, rather than as static equilibrium shapes, can select markedly smaller half-angles. In particular, Betelú *et al.* found a transient conical tip with a semi-angle near 27° in a charged viscous-drop calculation governed by a dynamic electric–viscous balance [28].

Compared with droplets, soap bubbles and soap films provide a thin-film, multi-interface platform in which electrohydrodynamic deformation can be studied in a comparatively simple geometry. Early experiments by Wilson and Taylor and by Macky documented bursting and deformation of soap bubbles in electric fields [29,30]. Related bubble and film problems include electrically stressed gas cavities in liquids, charged hemispherical soap bubbles, soap-film bridges, and, more recently, deformation of sessile and floating soap bubbles in a plane capacitor [31–35] and in nonuniform electrode configurations [36]. A related recent study also examined soap-bubble stream charging from analytical and experimental perspectives, extending the bubble-electrostatics literature beyond deformation alone [37]. These systems make the departure from the canonical droplet problem explicit. The interface is a thin film with two air–liquid surfaces. The substrate fixes the large-scale geometry. The background electric field is set by a finite electrode gap rather than by a self-similar conical field.

Recent soap-bubble experiments in plane-capacitor geometries established field-driven deformation, but they left open how the steady deformation regime ends and how the apex evolves in the final approach to jetting [34]. More broadly, the missing step is a unified experimental description that connects the stable branch, its end point, and the subsequent cone-forming and pre-jet stages within one soap-bubble system.

In this paper, we address that gap using a sessile soap bubble in a planar electric field. We first characterize the stable regime and ask whether the deformation can be organized by a single steady-state branch across initial bubble size when expressed in the dimensionless field $E^* = \mathrm{Bo}_e^{1/2}$ where $\mathrm{Bo}_e = \varepsilon_0 E_0^2 R_0/(2\gamma)$ compares electric stress with the capillary restoring stress of the soap film. We then identify the end point of that branch and track the subsequent conical sharpening up to jet emission. The main results are threefold. First, stable deformation is well represented by an ellipsoid-of-revolution geometry and, within a fixed ambient session, the data collapse onto a single steady-state branch relating the aspect ratio α to E^*. Second, the end point of that branch marks the transition to the unstable regime. Third, in the unstable regime, the system selects cone angles of $30.0° \pm 0.6°$, and a fixed reference vertex allows comparing pre-jet trajectories across bubble sizes, with a near-tip inertia-capillary model capturing the observed late-stage acceleration of the apex toward the reference vertex.

II. EXPERIMENTAL SYSTEM AND ANALYSIS METHODS

A. Experimental setup and electric-field protocol

The apparatus consisted of a 3D-printed PLA insulating fixture carrying copper electrodes in a nominal parallel-plate arrangement. The insulation was shaped so that only the opposing electrode faces were exposed to the active region. The electrode gap was adjustable during preliminary tests. All data reported here were acquired at a fixed gap $H = 50$ mm, chosen as a practical value that suppressed visible corona over the operating voltage range while still allowing the desired deformation and jetting responses. The lower electrode was grounded, and the high-voltage connection to the upper electrode was routed through a separate insulated compartment outside the imaging region to minimize perturbations of the field in the measurement zone.

A sessile soap bubble of measured initial radius R_0 was formed on the lower electrode beneath a square copper top plate of characteristic lateral size $L \approx 140$ mm (Fig. 1). Because the plate is much

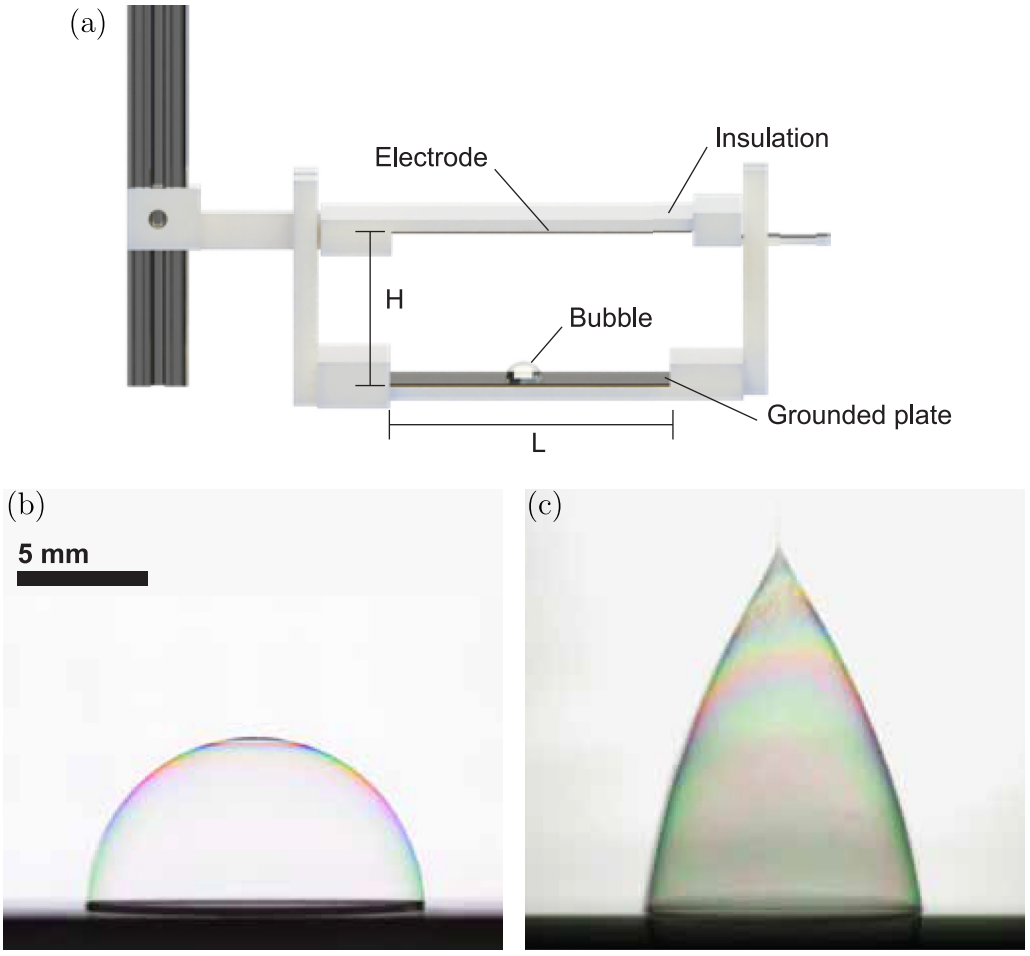

FIG. 1. (a) Schematic of experimental setting for a nominally uniform electric field configuration. A sessile soap bubble of measured radius R_0 is pinned on the lower electrode and placed a distance H below a top plate of width L. A nominal field of magnitude $E_0 \simeq V/H$ is applied and increased quasistatically. Representative side-view images illustrating the two response regimes: (b) smooth equilibrium deformation in the stable regime and (c) conical sharpening followed by jetting in the unstable regime.

larger than the bubble and the bubble was positioned near the plate center, the background field over the bubble-scale region is nominally uniform. We therefore use the nominal applied field

$$E_0 \equiv V/H, \tag{1}$$

where V is the applied potential difference. A Laplace calculation for the finite electrode geometry was used only to confirm that the field at the bubble location is well approximated by the parallel-plate estimate V/H. It was not used to determine the local field near the sharpened tip. A Laplace calculation for the exact electrode geometry is provided in Appendix D. Over the bubble-scale region beneath the plate center, the axial field differs from the parallel-plate estimate V/H by less than about 0.02%, which justifies the use of $E_0 = V/H$ as the nominal control parameter for the stable regime scaling.

Before inflation, an excess 2 μL sample of the soap solution was placed on the lower electrode to stabilize the contact region and reduce premature rupture. Air was then injected using a syringe

pump with prescribed input volume V_{in} to form a sessile bubble, and only cases in which the bubble remained centered beneath the top plate were retained for analysis. Although bubbles were generated with prescribed V_{in}, all analysis is based on the measured radius R_0 from images, because tubing compliance and bubble-formation dynamics can produce a mismatch between the pump setpoint and the measured bubble size. All subsequent nondimensionalization therefore uses the measured radius rather than the pump setpoint; the V_{in}-R_0 calibration is reported in Appendix A.

The voltage was increased quasistatically in discrete steps. In the stable regime, images were acquired only after the interface had relaxed to a stationary shape, and the voltage increment was refined near the stability limit. Beyond a critical field, the apex no longer relaxed to a smooth equilibrium but instead continued to sharpen toward jetting. The principal datasets used for the collapse analysis were acquired within the same experimental session for each size group.

B. Imaging and profile extraction

Side-view images were used to extract the meridional profile. Stable-regime shapes were recorded with a Nikon D7100 camera. Unstable-regime dynamics were recorded with a Photron FASTCAM NOVA S9 high-speed camera equipped with an AF Micro-NIKKOR 105 mm lens at 6000 fps with a shutter time of 5 μs. High-speed sequences were recorded from the onset of visible deformation through jet emission and rupture. The present analysis uses the prerupture interval relevant to cone formation and late pre-jet apex dynamics. Before each acquisition, a ruler was imaged in the same optical configuration to establish the pixel-to-length conversion.

Customized MATLAB scripts were used to measure the overall bubble height and width from the calibrated images. Custom Python scripts were used to extract the meridional profile for subsequent fitting and model comparison. The image-processing workflow therefore consisted of spatial calibration, profile extraction, and geometric fitting.

In the stable regime, the extracted meridional profile is well described by a prolate ellipsoid of revolution with vertical and horizontal semiaxes a and b, respectively, and the deformation is quantified by the aspect ratio

$$\alpha \equiv a/b. \tag{2}$$

The fitted meridional profile is written as

$$\frac{r^2}{b^2} + \frac{(z - z_c)^2}{a^2} = 1, \tag{3}$$

where z_c accounts for the vertical offset of the fitted profile. Here, $\alpha = 1$ corresponds to the undeformed reference state. The ellipsoid-of-revolution fit is used as a geometric description, not an exact free-boundary solution. Explicit closed-form expressions for the corresponding Taylor spheroidal equilibrium baselines [Fits I and II of Fig. 3(b)] are given in Appendix F.

In the unstable regime, the near-tip profile is fit locally by two straight segments defining a cone. The cone half-angle θ is measured between the cone side and the symmetry axis. To quantify the final pre-jet stage, we define a fixed reference vertex from the first frame with visible jet emission or, equivalently, from the last pre-jet frame in which the cone shapes are stationary. Specifically, local linear fits are applied to the near-tip cone shape in that reference frame, and the intersection of their extrapolated extensions defines the reference vertex. For each earlier frame, $\ell(t)$ is taken as the axial distance from the instantaneous apex to this fixed reference vertex. (We denote this pre-jet distance by ℓ to avoid any confusion with the horizontal semiaxis b of the stable-regime ellipsoid of revolution.) In high-speed videos, $t = 0$ denotes the first frame with visible jet emission.

C. Solution properties and dimensionless groups

Soap bubbles were prepared from an aqueous surfactant mixture of 63% deionized water, 30% glycerol, and 7% Dawn commercial dish soap by volume. A representative single-interface

TABLE I. Representative measured and adopted system parameters.

Quantity	Value (range)	Description
R_0	3–8 mm	Measured initial bubble radius
H	50 mm	Electrode gap
L	140 mm	Characteristic top-electrode lateral size
E_0	up to 10^5–10^6 V/m	Nominal applied field magnitude
γ	≈0.03 N/m	Single-interface surface tension; reduced capillary scale uses $2\gamma/R_0$
h	$h = O(10^2\,\mathrm{nm})$	Estimated film thickness; not measured *in situ*
ρ	≈1080 kg/m^3	Liquid density
ε_0	8.854×10^{-12} F/m	Vacuum permittivity

surface tension is taken as $\gamma \approx 0.03\,\mathrm{N/m}$, and the liquid density is taken as $\rho \approx 1080\,\mathrm{kg/m^3}$. Representative measured and adopted system parameters are summarized in Table I.

The film thickness h was not measured *in situ* during each run. We therefore use h only as a literature-based order-of-magnitude estimate when checking the thin-film condition $h \ll R_0$ and when setting the prefactor scale in the reduced apex-focusing model. Reported equilibrium soap-film thicknesses range from common black films of order 10–100 nm to Newton black films of order 5–10 nm, while very thin soap bubbles can approach limiting thicknesses of order 200 nm [38,39]. In view of this spread, we adopt $h = O(10^2\,\mathrm{nm})$ and use it only as a representative range. The stable-regime collapse and the regime classification do not rely on a direct measurement of h.

The reduced scaling used below is from the usual electrohydrodynamic free-boundary formulation [4,5,7]. In the gas region surrounding the bubble, the electric potential satisfies

$$\nabla^2\phi = 0, \qquad \mathbf{E} = -\nabla\phi, \tag{4}$$

and the corresponding Maxwell stress tensor is

$$\mathbf{T}_M = \varepsilon_0\big(\mathbf{E}\otimes\mathbf{E} - \tfrac{1}{2}E^2\mathbf{I}\big). \tag{5}$$

For a single deformable interface, the local normal stress balance takes the form

$$[\![-p\mathbf{I} + \mathbf{T}_M]\!]\cdot\mathbf{n} = \gamma\kappa\,\mathbf{n}, \tag{6}$$

where $\kappa = 1/R_1 + 1/R_2$ is the total curvature and γ is the surface tension of a single air–liquid interface [4,5,7]. For the present soap bubble, the film has two air–liquid interfaces, so the capillary restoring contribution enters the reduced scaling with an effective coefficient 2γ [29,30]. At the scaling level used here, the electric stress is therefore of order $\varepsilon_0 E_0^2$, whereas the restoring capillary stress is of order $2\gamma/R_0$. This is the origin of the factor 2γ used below in the electric–capillary control parameter. The factor of two reflects the two air–liquid surfaces of the film and follows the same convention adopted by Taylor for a soap film [2,29]; an alternative choice that also accounts for the two principal radii of curvature would replace 2γ by 4γ. Because this is a constant $O(1)$ prefactor in a scaling parameter, it rescales E^* by a fixed factor and does not affect the data collapse, the shape of the steady-state branch, or its end point. In the present experiments, $E_0 = V/H$ is used as the nominal background field, as justified by the finite-electrode Laplace calculation in Appendix D.

We therefore define the electric Bond number

$$\mathrm{Bo}_e \equiv \frac{\varepsilon_0 E_0^2 R_0}{2\gamma}, \tag{7}$$

and, for plotting convenience, its square root

$$E^* \equiv \sqrt{\mathrm{Bo}_e} = E_0\sqrt{\frac{\varepsilon_0 R_0}{2\gamma}}. \tag{8}$$

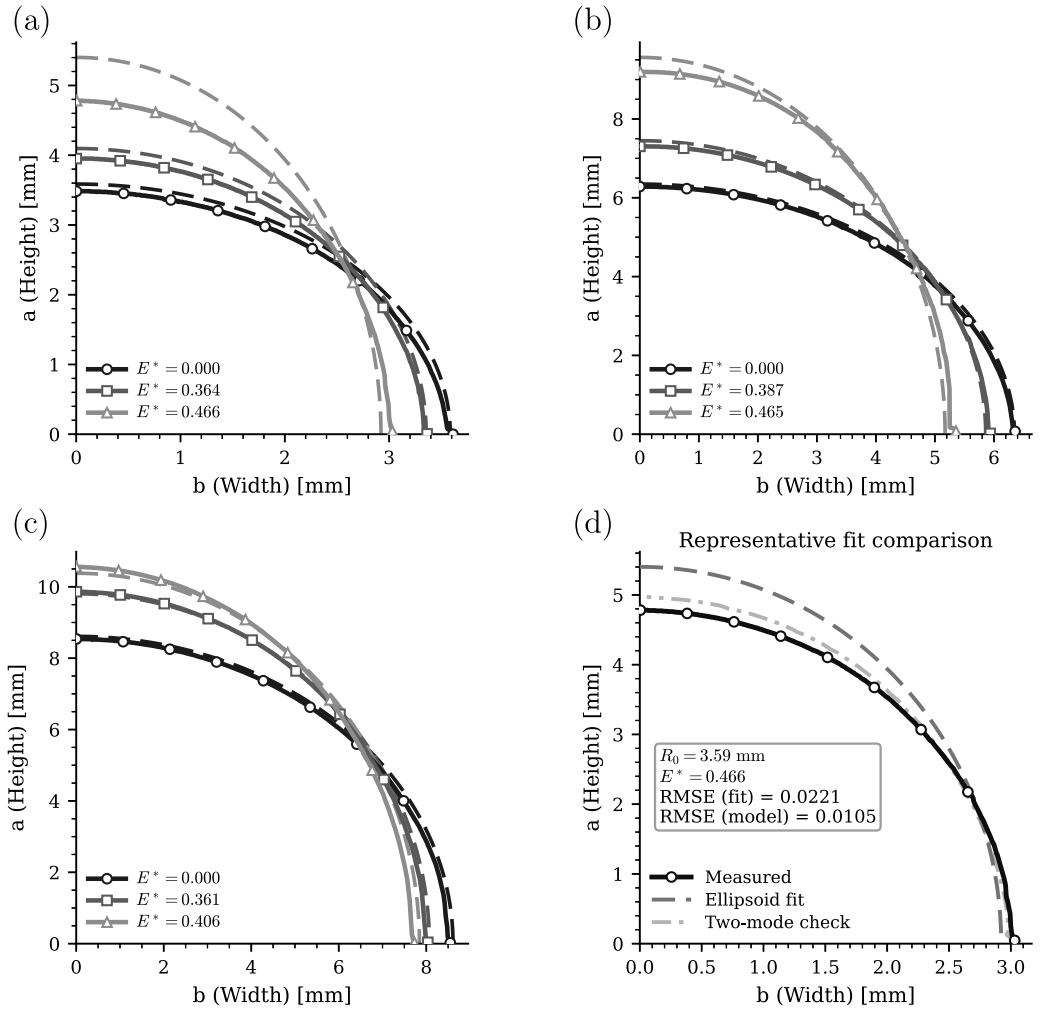

FIG. 2. Stable-regime profiles and ellipsoid-of-revolution representation. Panels (a)–(c) show representative small-, intermediate-, and large-bubble meridional profiles for $R_0 = 3.59$, 6.35, and 8.61 mm at several electric-field levels. Solid lines with markers denote measured profiles and dashed lines denote ellipsoid-of-revolution fits used to extract $\alpha = a/b$. Panel (d) shows a representative high-field stable small-bubble case together with the secondary two-mode reconstruction of Appendix B for a fit-accuracy check. The RMSE values in panel (d) correspond to this representative profile only.

All collapse plots in the present work use the measured R_0 from images rather than the pump setpoint V_{in}.

III. STABLE DEFORMATION AND TRANSITION TO INSTABILITY

A. Ellipsoid-of-revolution description of the steady profiles in the stable regime

In the stable regime, the bubble relaxes after each voltage increment to a smooth steady shape. Figure 2 shows representative meridional profiles for three initial-size groups. Over the measured electric-field range, the steady profiles along the branch are well represented by an ellipsoid-of-revolution fit, which provides both a one-parameter fit and a consistent deformation metric through $\alpha = a/b$. As noted in Sec. II B, the geometric fit serves as a deformation metric. A secondary

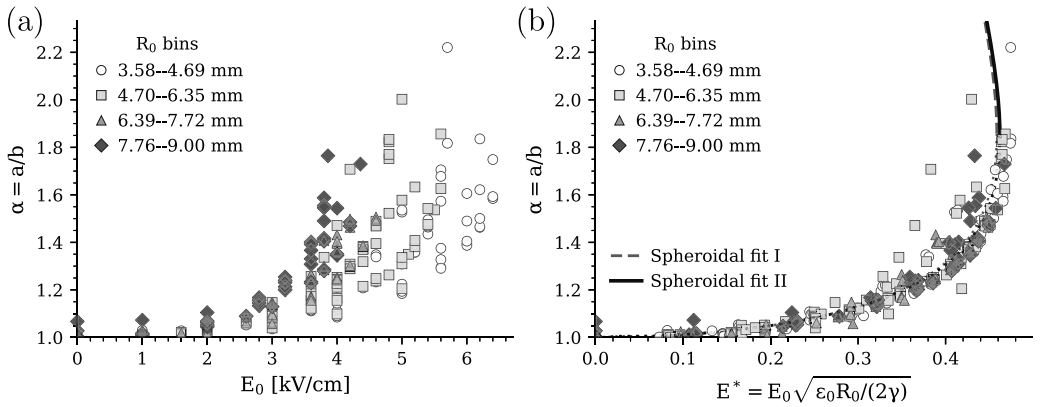

FIG. 3. (a) Stable-regime aspect ratio plotted against the nominal applied field E_0. The systematic offset among R_0 bins shows that the raw deformation data remain size dependent in E_0. (b) Stable regime collapse onto a single steady-state branch by replotting the same data against E^*. Aspect ratio α versus dimensionless field E^* collapses across multiple initial radii for data acquired within a single experimental session. The last observable steady states mark the end point of the branch and the transition to the unstable regime. The solid and dashed curves show two spheroidal baselines recast in the present normalization.

two-mode empirical reconstruction (Appendix B) yields only a marginal improvement in profile RMSE and is used solely as a fit-accuracy check, not in the main analysis.

B. Collapse onto a single steady-state branch and transition to instability

When α is plotted against E^*, data from multiple initial radii merge into a single steady-state branch within the tested range (Fig. 3). Over the tested size range and within a fixed ambient session, the deformation is organized primarily by electric stress relative to capillary pressure rather than by initial size alone.

The end point of the branch is identified by slowly ramping the voltage near onset and recording the point at which the apex ceases to relax to a smooth steady profile and instead sharpens continuously. We denote the corresponding transition field by E_c^*. Because α is single-valued on the steady-state branch, the same transition can equivalently be characterized by a corresponding aspect ratio $\alpha_c = \alpha(E_c^*)$. Over the tested size groups, the last observable steady states yield $E_c^* \approx 0.45$–0.47 and $\alpha_c \approx 1.8$–1.9. The narrow spread in E_c^* indicates that the branch end point depends only weakly on initial radius. The curve is reported for fixed ambient conditions in the present geometry. Control runs show that humidity shifts the branch between sessions, so E^* should be read here as the organizing dimensionless field for the present system under fixed ambient conditions, not a session-independent constitutive law.

C. Interpretive role of the spheroidal baseline for the steady-state branch

The full electrohydrodynamic free-boundary problem stated above is not solved exactly in the present finite-gap, sessile, and thin-film geometry. Instead, we use a Taylor-type spheroidal approximation as a reduced baseline for the stable regime. Here, 'Fit I' denotes the spheroidal approximation obtained from a local balance at the pole and equator, whereas 'Fit II' denotes the companion approximation based on an integrated balance over the interface. These are the Approximations I and II of Taylor [2], in which the Maxwell stress of Eq. (5) is balanced against surface tension and the internal pressure difference [Eq. (6)] on a prolate spheroid; we therefore use Eqs. (4)–(6) to generate the model curves, while the ellipsoid-of-revolution fit to the images

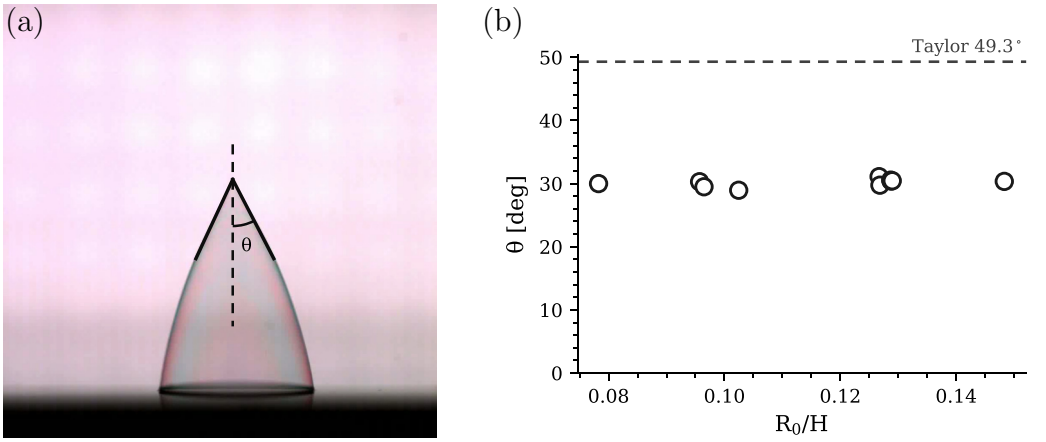

FIG. 4. Cone-angle selection in the unstable regime. (a) Definition of the cone half-angle θ from local linear fits to the near-tip sides in the last frame before jetting. (b) Measured cone half-angle θ plotted against R_0/H (equivalently, against the initial bubble size for fixed H). The dashed horizontal line marks the classical Taylor value 49.3° only as an external reference for the ideal conical equipotential construction. The range of R_0/H is restricted to $R_0/H \ll 1$ for the reasons discussed in the text; over the accessible range θ shows no systematic dependence on R_0/H.

remains a separate geometric extraction of $\alpha = a/b$. The explicit closed-form relations $\alpha(E^*)$ for both baselines, recast in the present normalization, are derived in Appendix F.

That baseline gives a one-parameter description of the steady-state branch and reduces the stable data to $\alpha(E^*)$. In many spheroidal models, the steady branch terminates at a limiting electric loading [2,15,17,18]. The experimentally observed last steady states qualitatively match such an end point, but the primary experimental result here is the collapsed branch itself, with the end point extracted from it.

IV. CONE FORMATION AND PRE-JET APEX DYNAMICS

A. Cone-angle selection for a transient pre-jet cone

Beyond the end point of the steady-state branch, or equivalently for $E^* > E_c^*$, the apex no longer approaches a steady, smooth shape but sharpens rapidly into a pointed tip that is locally well represented by a cone over a finite near-tip region. The measured cone half-angle lies in the range $\theta \approx 30.0^\circ \pm 0.6^\circ$, substantially below the classical Taylor value of 49.3° [Fig. 4(b)]. The reported angle range reflects both variation between experiments and the fact that the measured angle depends somewhat on which visible part of the cone side was used for the line fit. The cone angle is reproducibly selected in the sessile-bubble geometry under a parallel-plate electric field with weak dependence on R_0/H.

This result does not contradict Taylor's conical construction [2]. Taylor's 49.3° half-angle is the semi-angle of a static equilibrium cone, obtained from a specific electrostatic construction for an equipotential conical surface in a compatible field, and self-similar analyses of cone formation on conducting liquids recover this angle as the asymptotic attractor for that equilibrium problem [40]. The cones recorded here, by contrast, are not static equilibrium shapes. The apex sharpens continuously toward jet emission, so the local balance can involve inertial and viscous stresses, thin-film motion, charge transport, and the evolving near-tip electric field rather than Taylor's static capillary–electrostatic balance. Once a cone is fully formed, the near-tip field becomes much larger than the imposed background field, so the observed half-angle should not be attributed to the externally imposed field geometry alone. This interpretation is consistent with the dynamic

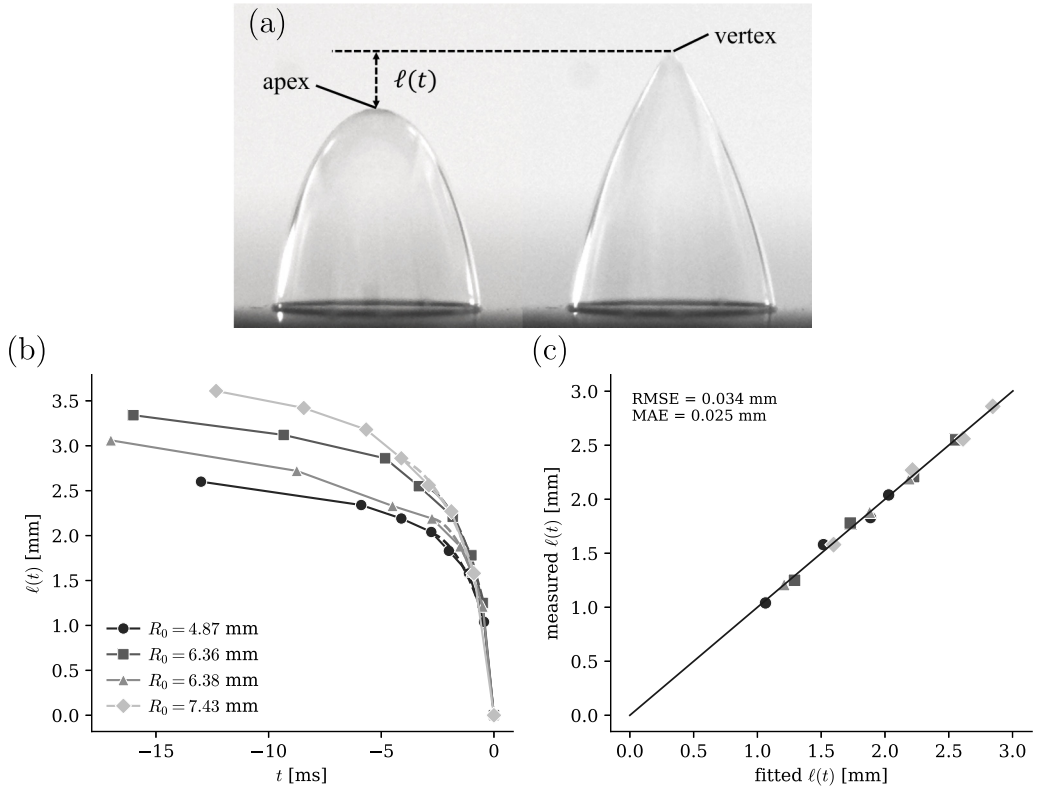

FIG. 5. Unstable kinematics at the pre-jet stage. (a) Definition of the fixed reference vertex and the apex-to-reference-vertex distance $\ell(t)$. The reference vertex is determined from the first frame with visible jet emission by extrapolating the near-tip. The distance $\ell(t)$ for earlier frames is then measured from the instantaneous apex to this fixed reference point. (b) Temporal evolution of the apex-to-reference-vertex distance $\ell(t)$ with time aligned so that $t = 0$ marks the first frame with visible jet emission. (c) Comparison between measured ℓ and fitted ℓ for the points included in the fit in panel (b). The diagonal line indicates perfect agreement.

calculation of Betelú *et al.*, where a charged viscous drop develops a transient conical tip with a semi-angle near 27° under an electric–viscous balance [28]. The present soap-film problem is different, but the comparison supports interpreting the measured $30.0^\circ \pm 0.6^\circ$ as a dynamically selected pre-jet angle rather than as a modified static Taylor angle.

The accessible range of R_0/H in Fig. 4(b) is limited by the fixed-gap geometry and by the need to keep the bubble centered, pinned, and well separated from the upper electrode so that $E_0 = V/H$ remains a meaningful nominal control parameter. In this setup, larger bubbles were less reproducible and more prone to premature rupture. We therefore use Fig. 4(b) to document the observed scatter in θ, not to establish a systematic R_0/H scaling law.

B. Apex approach before jetting

To quantify the final sharpening stage, we define a fixed reference vertex from the first frame with visible jet emission, or equivalently from the last pre-jet frame for which the cone side profiles are stationary. Specifically, local linear fits are applied to the near-tip conical profile in that reference frame, and their extrapolated intersection defines the reference vertex, as shown in Fig. 5(a). For each earlier frame, $\ell(t)$ is the axial distance from the instantaneous apex to this fixed reference vertex. With this definition, $\ell(t)$ decreases rapidly as jetting is approached, while the local curvature

scale grows approximately as $\kappa \sim 1/\ell$. Time is aligned so that $t = 0$ marks the first frame with visible jet emission. The point closest to visible jet emission is the most sensitive to the choice of reference frame and to the line fit of the cone side, so it is excluded from the direct fit in Fig. 5(b) and from the parity plot comparing data with the model in Fig. 5(c).

The data in Fig. 5(b) show that ℓ decreases rapidly during the final measured interval before visible jet emission. To interpret that trend, we use a local force balance adapted from Taylor's original calculation of the motion of a conical soap-film interface toward its vertex [2], together with ideas from capillary–inertial singularity dynamics [41,42] and self-similar analyses of electrified tip formation [40]. The present balance is the thin-film inertia-capillary balance written by Taylor in his Eqs. (36) and (37) [2]. The transient cone angle and the late apex approach should be regarded as distinct measurements. Betelú *et al*. show that a dynamic electric–viscous balance can select a non-Taylor angle in a different charged-drop problem, whereas the relation below is an inertia-capillary scaling for the measured approach of $\ell(t)$. Thus, Eq. (10) characterizes the approach only and does not set the cone angle. In this balance, the film carries an effective areal mass $m \sim \rho h$, and the restoring capillary force scales with curvature as $1/\ell$. This balance is used here only to test whether the measured decrease of ℓ is consistent with the logarithmic form implied by Eq. (10) when the comparison is performed directly in the time domain.

A local force balance then takes the form

$$\rho h \frac{d^2\ell}{dt^2} \simeq -K\frac{\gamma}{\ell}, \tag{9}$$

where K is a dimensionless coefficient that collects the near-tip electric contribution into an effective prefactor. Multiplying Eq. (9) by $d\ell/dt$ and integrating gives

$$\left|\frac{d\ell}{dt}\right| \sim \left(\frac{2K\gamma}{\rho h}\right)^{1/2}\left[\ln\left(\frac{\ell_0}{\ell}\right)\right]^{1/2}, \tag{10}$$

where ℓ_0 is an outer cutoff of order R_0. Equation (10) predicts a weak logarithmic increase in the rate of decrease of ℓ as $\ell \to 0$. Since the local near-tip field is not known, we do not interpret the prefactor quantitatively. Instead, we compare the measured $\ell(t)$ trajectories with the integrated form of Eq. (10). Figure 5(c) shows the corresponding comparison between the measured data and the prediction for the points used in the fit.

As $\ell(t)$ approaches zero, the apex emits a thin axial jet, visible in Fig. 1(c), which is rapidly followed by film retraction and rupture. This jet is the natural end point of the pre-jet approach analyzed here and parallels the jet documented in Taylor's original soap-film observations [2]. A representative high-speed sequence of the emission event is provided in Appendix E. We use the first jet-emission frame as the terminal reference for the pre-jet dynamics, but do not analyze the post-emission jet diameter, breakup, or droplet production in the present work.

V. DISCUSSION

The stable-regime measurements show that the primary experimental result is the collapse of the aspect ratio onto a single steady-state branch $\alpha(E^*)$ across the tested initial radii within a fixed ambient session. In that sense, the transition field is not an independent parameter but the end point of the observed branch. Beyond that end point, the system enters a regime of conical sharpening and rapid apex approach before jetting. For conducting sessile drops in parallel-plate fields, Basaran and Scriven [17,18] computed steady branches with turning points corresponding to terminal aspect ratios in the range $\alpha_c \approx 1.8$–1.9, depending on contact angle and electrical boundary conditions. The terminal aspect ratios measured here are close to $\alpha_c \approx 1.9$, despite the present interface being a soap film with two air–liquid surfaces rather than a bulk liquid drop. This agreement supports the use of the electric Bond number as a useful organizing parameter for the stable branch at the scaling level adopted here, while not implying that the present thin-film geometry is dynamically equivalent to the conducting-drop problem.

That qualification is important because the nondimensionalization uses the nominal background field $E_0 = V/H$, and the film thickness and electrical properties of the solution have not been measured directly. These limitations do not alter the empirical observations themselves, namely, the collapsed steady-state branch, the operationally identified transition field, the measured cone-angle range, or the observed pre-jet trajectories in $\ell(t)$. They do, however, limit how far the present measurements can be pushed toward full mechanistic closure. In particular, a self-consistent calculation of the evolving near-tip electric field, together with *in situ* film-thickness measurement and direct characterization of conductivity, would be needed to connect the measured trajectories more tightly to a predictive electrohydrodynamic model.

The measured cone half-angle of $30.0^\circ \pm 0.6^\circ$ is substantially smaller than Taylor's 49.3°. As discussed in Sec. IV A, we interpret this primarily as a dynamic pre-jet angle: Taylor's value is the semi-angle of a static equilibrium cone, whereas the present cone sharpens continuously toward jet emission. The dynamic calculation of Betelú *et al.* provides a relevant comparison because it selects a smaller transient angle from an electric–viscous balance rather than from Taylor's static capillary–electrostatic balance [28]. Yarin *et al.* [23] similarly reported half-angles of about 33.5° for polymer-solution jets in a parallel-capacitor configuration and interpreted the departure from 49.3° in terms of boundary conditions that do not satisfy the self-similar assumptions behind Taylor's construction. In the present sessile-bubble geometry, the interface is additionally pinned to a substrate, the imposed field is set by a finite plate gap, and the soap-film potential was not measured directly; these factors may contribute to the precise value selected. Whether the remaining difference between about 30° here and about 33.5° in Ref. [23] reflects thin-film structure, contact conditions, or different fluid properties remains open.

The humidity sensitivity documented in Appendix C further shows that the steady-state branch is conditional on ambient conditions. In the control runs, lower ambient humidity shifts the deformation curve to a higher nominal electric field. This trend is consistent with humidity-dependent evolution of the soap film during the voltage ramp, although the present measurements do not isolate the responsible mechanism. Possible contributors include evaporation-driven thinning, changes in charge-relaxation behavior, and changes in permittivity in the surrounding dielectric medium. Resolving their relative importance would require *in situ* thickness measurements and electrical characterization during the field ramp.

The same distinction between empirical organization and predictive closure applies to Eq. (10). The logarithmic form contains quantities such as K, ℓ_0, and h that are not independently determined here, so its value is diagnostic rather than predictive. What the comparison in Fig. 5 establishes is that the measured $\ell(t)$ trajectories are consistent with a reduced near-tip inertia-capillary balance at a shrinking tip. Equation (10) should therefore be read as a reduced law for the measured pre-jet trajectories, not as a predictive cone-jet theory. A predictive model would require a self-consistent treatment of the evolving near-tip electric field coupled to thin-film charge transport.

VI. CONCLUSIONS

We studied sessile soap bubbles driven by a nominally uniform electric field and identified two reproducible response regimes within one experimental geometry. In the stable regime, the meridional profile is well represented by an ellipsoid of revolution, and the data reduce to a single curve when plotted against the dimensionless field $E^* = \sqrt{\mathrm{Bo}_e}$ for data acquired within a fixed ambient session. The end point of this branch defines the transition to the unstable regime. Beyond that transition, the interface develops a pointed tip and then a cone with half-angle $30.0^\circ \pm 0.6^\circ$, below the classical Taylor value and interpreted here as a dynamic pre-jet angle rather than as a static Taylor-cone angle. A fixed reference vertex provides a practical reference for comparing the late stage before jetting across bubble sizes. The measured decrease of $\ell(t)$ accelerates as jetting is approached, and a reduced near-tip inertia-capillary model captures the observed logarithmic trend in that rate.

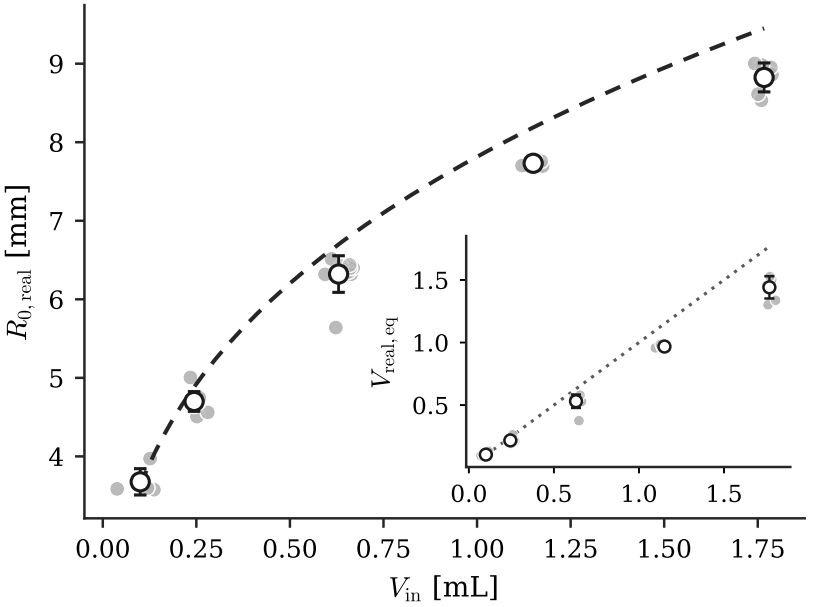

FIG. 6. Calibration between pump input volume V_{in} and the measured initial bubble size. Gray symbols denote individual runs, and open circles with error bars indicate the mean ± standard deviation of the measured initial radius $R_{0,\mathrm{real}}$ for each input setting. The dashed curve is the hemispherical-equivalent radius associated with the pump input volume. Inset shows the hemispherical-equivalent volume estimated from the measured initial radius. The dotted line is the identity. All subsequent analysis uses the measured $R_{0,\mathrm{real}}$.

ACKNOWLEDGMENTS

This work was supported by a graduate fellowship from SK Innovation Co., Ltd. The authors thank Crystal R. Fowler for her ideas and knowledge to develop this project. H.K. and S.J. conceived the idea and designed the experiment. H.K. built the experimental setup, collected and analyzed data, interpreted the results, and wrote the manuscript. H.K. and S.J. revised the manuscript.

The authors have no competing interests.

DATA AVAILABILITY

The data that support the findings of this article are openly available [43].

APPENDIX A: PUMP-VOLUME CALIBRATION

Figure 6 reports the calibration between the prescribed pump input volume V_{in} and the measured initial radius R_0 used throughout the nondimensionalization.

APPENDIX B: SECONDARY FIT-ACCURACY CHECK

As a fit-accuracy check, Fig. 2(d) compares the measured meridional profile with the ellipsoid-of-revolution fit and with a secondary two-mode empirical reconstruction referenced to the zero-field profile of the same bubble,

$$y(E^*) \approx y_0 + c_1(E^*)\psi_1 + c_2(E^*)\psi_2. \tag{B1}$$

Here, ψ_1 and ψ_2 are empirical shape functions extracted from the stable-regime dataset. Over all stable cases with the field on, this representation reduces the median normalized-profile RMSE

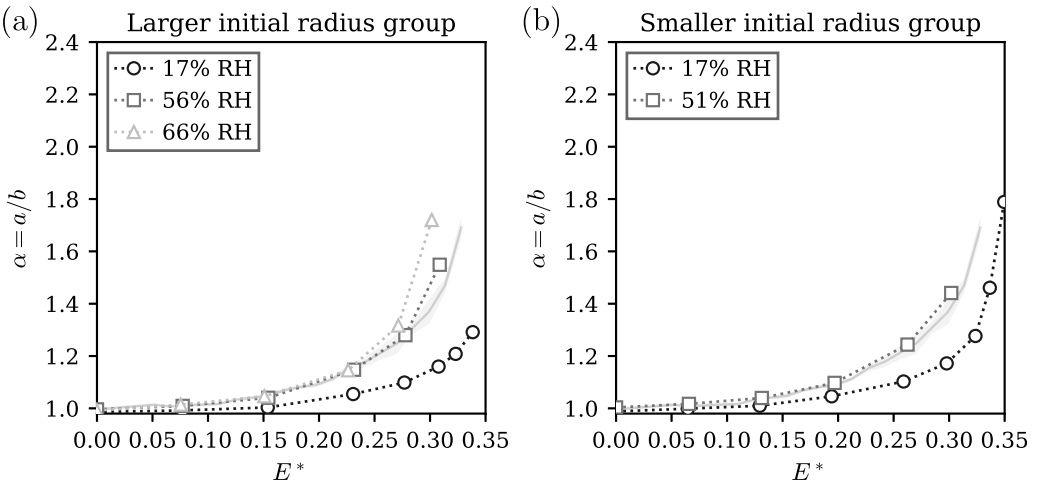

FIG. 7. Humidity-control measurements for the stable regime. Panel (a) shows the larger initial-radius group and panel (b) shows the smaller initial-radius group. The shift of the deformation curve with relative humidity indicates that the collapsed steady-state branch in Fig. 3 is conditional on the ambient condition of a given session. The thin gray band indicates the reference stable branch obtained from the main steady-state dataset and is shown only as a background for comparison.

from 0.0135 to 0.0102. Because the improvement is modest and because the coefficients are purely empirical, the two-mode reconstruction is not used in the main analysis; the ellipsoid-of-revolution fit and the aspect ratio $\alpha = a/b$ remain the primary deformation metric.

APPENDIX C: OPERATIONAL DEFINITIONS AND HUMIDITY SENSITIVITY

Near the transition to the unstable regime, the voltage was increased slowly from the highest clearly stable condition, and the onset of persistent sharpening was recorded directly. We take that onset value as E_c^*, with uncertainty set by the voltage readout resolution near onset together with the finite sensitivity in identifying the first persistent departure from steady relaxation. In the main text, this onset is interpreted as the end point of the steady-state branch in Fig. 3.

A similar operational issue enters the unstable regime metric. The fixed reference vertex is determined from the first frame with visible jet emission, or equivalently from the last pre-jet frame for which the cone shapes are stationary. The data point nearest jet emergence is excluded from the direct fit and from the parity plot because it is the most sensitive to the selected reference frame, finite frame rate, and the line fit to the cone side.

Separate control experiments show that lower ambient humidity shifts the deformation curve to higher nominal electric field (Fig. 7). Because several coupled mechanisms could contribute, including changes in permittivity of the medium, which is air in this case, charge relaxation, and evaporation-driven film evolution, humidity is treated here as an experimental control variable.

APPENDIX D: FINITE-ELECTRODE LAPLACE CALCULATION FOR THE NOMINAL BACKGROUND FIELD

To assess how closely the experimental geometry approximates a parallel-plate field, we solved Laplace's equation for the finite electrode configuration used in the experiment. The purpose of this calculation is limited to the nominal background field over the bubble-scale region beneath the plate center. It is not used to estimate the local field in the apex region during conical sharpening or jetting.

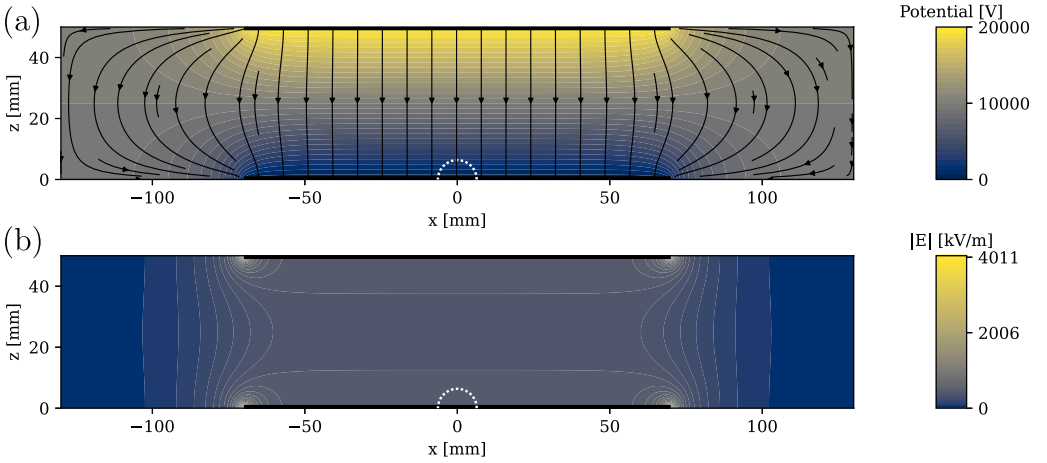

FIG. 8. Finite-electrode Laplace calculation for the experimental geometry. (a) Electric potential and representative field lines. (b) Electric-field magnitude. The dashed semicircle marks a representative bubble-scale guide centered beneath the top plate. It is a geometric guide for post-processing only and is not included in the Laplace solve. Evaluated along this guide, the axial field differs from the parallel-plate estimate V/H by less than about 0.02%, supporting the use of $E_0 = V/H$ as the nominal field in the main-text stable-regime scaling.

Figure 8(a) shows the electric potential and representative field lines for the imposed finite-electrode geometry, and Fig. 8(b) shows the corresponding electric-field magnitude. Because the quantity relevant to the nondimensionalization is the imposed axial background field, the comparison with the nominal estimate V/H is made from the axial component extracted from the same Laplace solution along the representative bubble-scale guide indicated in Fig. 8.

Over that bubble scale region, the axial field differs from the parallel-plate estimate V/H by less than about 0.02%, with a mean deviation of about $+0.02\%$. This supports the use of $E_0 = V/H$ as the nominal applied field in the stable-regime scaling. The dashed semicircle in Fig. 8 is a geometric guide for this post-processing comparison only and is not included in the Laplace solve.

APPENDIX E: SEQUENCE OF JET EMISSION

Figure 9 provides a representative high-speed sequence of the jet-emission event following conical sharpening. The sequence is included to document the axial jet visible at the cone apex and to clarify the terminal event used to define the end of the pre-jet approach. The post-emission dynamics, including jet thinning, breakup, droplet production, and film retraction, are not analyzed quantitatively in the present work.

APPENDIX F: SPHEROIDAL EQUILIBRIUM BASELINES

The model curves labeled Fit I and Fit II in Fig. 3(b) are Taylor's spheroidal Approximations I and II [2] for an uncharged conducting interface in a uniform field, evaluated for the present soap-film capillary scaling. They are obtained by balancing the Maxwell stress of Eq. (5) against surface tension and the internal pressure difference [Eq. (6)] on a prolate spheroid of constant volume, and are quoted here only to provide a physically based reference branch; they are not free-boundary solutions of the present finite-gap, sessile, thin-film problem.

Let the axial section of the spheroid be $x^2/a^2 + y^2/b^2 = 1$ with major semiaxis a and minor semiaxis b. To avoid confusion with the experimentally reported aspect ratio, define Taylor's internal

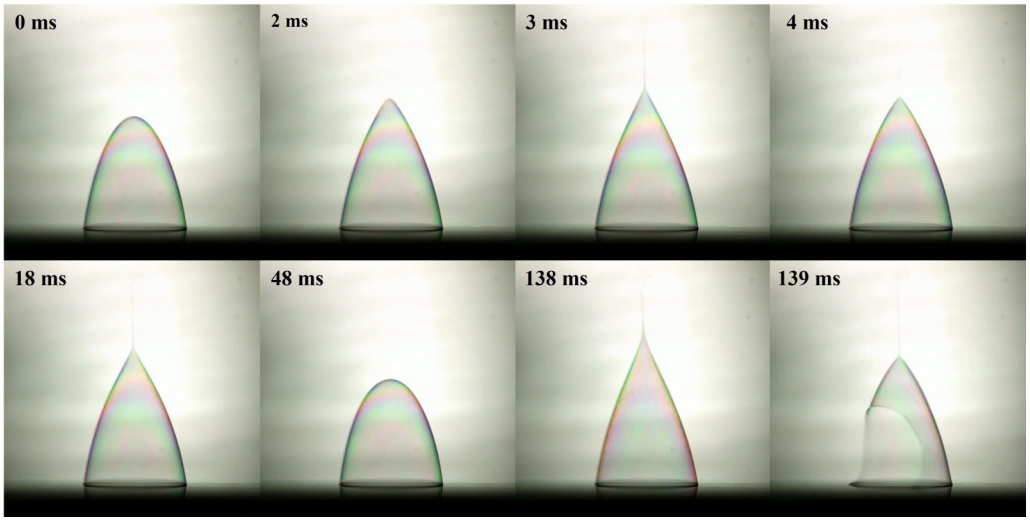

FIG. 9. High-speed image sequence documenting the jet-emission event following conical sharpening. The images were recorded at 6000 fps, and the time labels are measured from the first image shown above. The sequence shows the transition from the terminal pre-jet cone to axial jet emission and subsequent film retraction/rupture. For clarity, intermediate frames showing repeated upward and downward oscillations and multiple jet-emission events are omitted. The present study uses the jet-emission event as the terminal reference for the pre-jet dynamics, whereas quantitative analysis of the post-emission jet and droplet breakup is left for future work.

spheroidal parameter

$$q = 1 - e^2 = \frac{b^2}{a^2}, \quad \alpha = \frac{a}{b} = q^{-1/2}, \tag{F1}$$

where e is the eccentricity and α is the aspect ratio used in the main text. The standard spheroidal field integral for the uncharged-spheroid problem is

$$I_2 = \frac{1}{2e^3} \ln \frac{1+e}{1-e} - \frac{1}{e^2}. \tag{F2}$$

For an uncharged spheroid in a uniform field, Taylor's Approximation I gives

$$F r_0^{1/2} T^{-1/2} = (8\pi)^{1/2} M(q) I_2, \quad M(q) = q^{2/3}(2 - q^{1/2} - q^{3/2})^{1/2}, \tag{F3}$$

where the pointwise equilibrium conditions are satisfied at the pole and the equator. Taylor's Approximation II, based on the integrated equatorial balance, gives

$$F^2 r_0 T^{-1} = 16\pi q^{1/3}(1 - q^{1/2}) I_2^2 / \phi(e), \quad \phi(e) = \frac{1}{1-e^2} + \frac{1}{e^4}[e^2 + \ln(1-e^2)]. \tag{F4}$$

Here, F is the applied field, r_0 the equivalent undeformed radius, and T the surface tension in Taylor's notation. Equations (F3) and (F4) reproduce Taylor's Eqs. (19) and (20), while Eq. (F1) converts the parameter q to the main-text aspect ratio $\alpha = a/b$.

To place these baselines in the present normalization, we identify the deforming field with E_0, the equivalent radius with R_0, and the capillary scale with that of the two-sided soap film, $T \to 2\gamma$. Both relations then map onto the dimensionless loading

$$E^* = E_0 \sqrt{\frac{\varepsilon_0 R_0}{2\gamma}}, \tag{F5}$$

up to the constant electrostatic prefactor associated with the unit convention. Thus Eqs. (F3) and (F4) each define a reference branch $\alpha(E^*)$. These are the solid and dashed curves in Fig. 3(b). Both branches rise steeply and terminate near $\alpha \approx 1.8$–1.9, matching the limiting-loading end point discussed in Sec. III C.

We emphasize that this Appendix supplies the explicit model curves only; the primary experimental result of the main text is the empirical collapse of α onto a single branch, with the end point extracted from the data.

[1] J. Zeleny, Instability of electrified liquid surfaces, Phys. Rev. **10**, 1 (1917).
[2] G. I. Taylor, Disintegration of water drops in an electric field, Proc. R. Soc. London A **280**, 383 (1964).
[3] G. I. Taylor, Studies in electrohydrodynamics. I. The circulation produced in a drop by an electric field, Proc. R. Soc. London A **291**, 159 (1966).
[4] J. R. Melcher and G. I. Taylor, Electrohydrodynamics: A review of the role of interfacial shear stresses, Annu. Rev. Fluid Mech. **1**, 111 (1969).
[5] D. A. Saville, Electrohydrodynamics: The Taylor–Melcher leaky dielectric model, Annu. Rev. Fluid Mech. **29**, 27 (1997).
[6] J. Fernández de la Mora, The fluid dynamics of Taylor cones, Annu. Rev. Fluid Mech. **39**, 217 (2007).
[7] P. M. Vlahovska, Electrohydrodynamics of drops and vesicles, Annu. Rev. Fluid Mech. **51**, 305 (2019).
[8] A. M. Ganan-Calvo, J. M. Lopez-Herrera, M. A. Herrada, A. Ramos, and J. M. Montanero, Review on the physics of electrospray: From electrokinetics to the operating conditions of single and coaxial Taylor cone-jets, and ac electrospray, J. Aerosol Sci. **125**, 32 (2018).
[9] M. Cloupeau and B. Prunet-Foch, Electrostatic spraying of liquids in cone-jet mode, J. Electrost. **22**, 135 (1989).
[10] I. Hayati, A. I. Bailey, and T. F. Tadros, Mechanism of stable jet formation in electrohydrodynamic atomization, Nature (London) **319**, 41 (1986).
[11] A. Gomez and K. Tang, Charge and fission of droplets in electrostatic sprays, Phys. Fluids **6**, 404 (1994).
[12] A. Barrero and I. G. Loscertales, Micro- and nanoparticles via capillary flows, Annu. Rev. Fluid Mech. **39**, 89 (2007).
[13] A. Jaworek, Electrospray droplet sources for thin film deposition, J. Mater. Sci. **42**, 266 (2007).
[14] A. Jaworek and A. T. Sobczyk, Electrospraying route to nanotechnology: An overview, J. Electrost. **66**, 197 (2008).
[15] S. Torza, R. G. Cox, and S. G. Mason, Electrohydrodynamic deformation and bursts of liquid drops, Philos. Trans. R. Soc. A **269**, 295 (1971).
[16] J. D. Sherwood, Breakup of fluid droplets in electric and magnetic fields, J. Fluid Mech. **188**, 133 (1988).
[17] O. A. Basaran and L. E. Scriven, Axisymmetric shapes and stability of charged drops in an external electric field, Phys. Fluids A **1**, 799 (1989).
[18] O. A. Basaran and L. E. Scriven, Axisymmetric shapes and stability of pendant and sessile drops in an electric field, J. Colloid Interface Sci. **140**, 10 (1990).
[19] F. K. Wohlhuter and O. A. Basaran, Shapes and stability of pendant and sessile dielectric drops in an electric field, J. Fluid Mech. **235**, 481 (1992).
[20] O. Vizika and D. A. Saville, The electrohydrodynamic deformation of drops suspended in liquids in steady and oscillatory electric fields, J. Fluid Mech. **239**, 1 (1992).
[21] E. Lac and G. M. Homsy, Axisymmetric deformation and stability of a viscous drop in a steady electric field, J. Fluid Mech. **590**, 239 (2007).
[22] H. A. Stone, J. R. Lister, and M. P. Brenner, Drops with conical ends in electric and magnetic fields, Proc. R. Soc. London, Ser. A **455**, 329 (1999).
[23] A. L. Yarin, S. Koombhongse, and D. H. Reneker, Taylor cone and jetting from liquid droplets in electrospinning of nanofibers, J. Appl. Phys. **90**, 4836 (2001).

[24] R. T. Collins, J. J. Jones, M. T. Harris, and O. A. Basaran, Electrohydrodynamic tip streaming and emission of charged drops from liquid cones, Nat. Phys. **4**, 149 (2008).
[25] R. T. Collins, K. Sambath, M. T. Harris, and O. A. Basaran, Universal scaling laws for the disintegration of electrified drops, Proc. Natl. Acad. Sci. USA **110**, 4905 (2013).
[26] A. Ramos and A. Castellanos, Conical points in liquid-liquid interfaces subjected to electric fields, Phys. Lett. A **184**, 268 (1994).
[27] S. N. Reznik, A. L. Yarin, A. Theron, and E. Zussman, Transient and steady shapes of droplets attached to a surface in a strong electric field, J. Fluid Mech. **516**, 349 (2004).
[28] S. I. Betelú, M. A. Fontelos, U. Kindelán, and O. Vantzos, Singularities on charged viscous droplets, Phys. Fluids **18**, 051706 (2006).
[29] C. T. R. Wilson and G. I. Taylor, The bursting of soap-bubbles in a uniform electric field, Math. Proc. Camb. Phil. Soc. **22**, 728 (1925).
[30] W. A. Macky, The deformation of soap bubbles in electric fields, Math. Proc. Cambridge Philos. Soc. **26**, 421 (1930).
[31] C. G. Garton and Z. Krasucki, Bubbles in insulating liquids: Stability in an electric field, Proc. R. Soc. London A **280**, 211 (1964).
[32] J. E. Hilton and A. van der Net, Dynamics of charged hemispherical soap bubbles, EPL (Europhysics Letters) **86**, 24003 (2009).
[33] D. E. Moulton and J. A. Pelesko, Theory and experiment for soap-film bridge in an electric field, J. Colloid Interface Sci. **322**, 252 (2008).
[34] S. Mawet, H. Caps, and S. Dorbolo, Deformation of soap bubbles in uniform electric fields, Phys. Rev. Fluids **6**, 043603 (2021).
[35] S. Mawet, H. Caps, S. Dorbolo, and F. Elias, Deformation of soap bubbles in uniform magnetic fields, Soft Matter **19**, 8318 (2023).
[36] A. Pelesz, K. Kapral, and P. Żyłka, Soap bubbles deformation in non-uniform electric field and corona discharge, J. Electrost. **122**, 103785 (2023).
[37] A. Pelesz and P. Żyłka, On analytical and experimental aspects of soap bubble stream charging, Exp. Fluids **61**, 241 (2020).
[38] L. J. Evers, E. J. Nijman, and G. Frens, The role of structure in rupturing Newton-black soap films: Dynamics of a molecular bilayer, Colloids Surf. A **149**, 521 (1999).
[39] E. Chatzigiannakis, N. O. Jaensson, and J. Vermant, Thin liquid films: Where hydrodynamics, capillarity, surface stresses and intermolecular forces meet, Current Opinion in Colloid & Interface Science **53**, 101441 (2021).
[40] N. M. Zubarev, Formation of conic cusps at the surface of liquid metal in electric field, Jetp Lett. **73**, 544 (2001).
[41] J. Eggers, Nonlinear dynamics and breakup of free-surface flows, Rev. Mod. Phys. **69**, 865 (1997).
[42] J. Eggers and M. A. Fontelos, *Singularities: Formation, Structure, and Propagation*, Cambridge Texts in Applied Mathematics No. 53 (Cambridge University Press, Cambridge, England, 2015)
[43] H. Kim and S. Jung, Data for "Deformation and instability of sessile soap bubbles in an electric field," OSF, 2026, https://doi.org/10.17605/OSF.IO/9C3ER.